CrystEngComm

Accepted Manuscript

ROYAL SOCIETY OF CHEMISTRY

www.rsc.org/crystengcomm

CrystEngComm

ARTICLE

Hydrothermal Synthesis and Photoluminescence Properties of $Ca_9Eu(PO_4)_7$ nanophosphors

Received 00th January 20xx,
Accepted 00th January 20xx

DOI: 10.1039/x0xx00000x

www.rsc.org/

Jiacheng Sun, Xiaoyun Mi*, Lijian Lei, Xiaoying Pan, Shuyi Chen, Zan Wang, Zhaohui Bai, Xiyan Zhang

The red-emitting $Ca_9Eu(PO_4)_7$ nanophosphors have been successfully synthesized by a facile hydrothermal method. X-ray diffraction (XRD), photoluminescence (PL) spectroscopy, GSAS structural refinement and scanning electron microscopy (SEM) were used to characterize the materials. Rietveld refinement of powder X-ray diffraction patterns of $Ca_9Eu(PO_4)_7$ demonstrated that the structure of $Ca_9Eu(PO_4)_7$ consisted of $[PO_4]$ tetrahedra, and Ca/Eu atoms filled in the space between the tetrahedral groups, with Eu^{3+} distributing randomly on three individual Ca crystallographic sites. The major red emission peak located at 616nm under 397nm excitation attributed to the electric dipole transition $^5D_0 \rightarrow {}^7F_2$ of Eu^{3+} was a parity forbidden f-f configuration transition, which would only occur when Eu^{3+} occupied lattice sites without inversion symmetry. Introducing Gd, La, Y ions into samples made luminescence properties of $Ca_9Eu_{1-x}Ln_x(PO_4)_7$ (Ln= Gd, La, Y) phosphors decrease. The pH value played a key role in the formation of $Ca_9Eu(PO_4)_7$ nanophosphor morphologies. With increasing pH values in the initial reaction solution, the morphologies of samples changed from rods to spheres and their aspect ratios decreased at the same time. Different morphologies have different photoluminescence properties, and samples prepared at pH 7 manifested better photoluminescence properties relative to other samples. Therefore, this novel red-emitting phosphor could be applied in white light-emitting diodes.

1. Introduction

White light-emitting diodes (W-LEDs) have drawn much attention in the lighting market in global energy shortages field[1,2] because it has good performance such as environmental friendliness, energy saving, high brightness and long lifetime.[3,4] Currently, the commercial white light is combining a yellow-emitting phosphor ($YAG:Ce^{3+}$) with a blue LED chip (~460nm).[5] However, this combination has a low color rendering index (CRI, Ra) due to the lack of red-light contribution and a high color temperature (T_c>4000K),[5,6] which limits the applications of this phosphor in certain medical applications and architectural lighting purposes. In order to overcome the disadvantage of this combination, an alternative way is to combine red/green/blue (RGB) phosphors with NUV InGaN-based LEDs, or to combine a blue LED with red/green phosphors to generate white light. However, the commercial sulfide-based red phosphors ($Y_2O_2S:Eu^{3+}$, $SrS:Eu^{2+}$ and $CaS:Eu^{2+}$)[7,8] have low chemical stability, low efficiency and short lifetime compared with blue and green phosphors. In order to improve the efficiency and lifetime of W-LEDs, a new red phosphor with high efficiency and excellent chemical stability needs to be developed.

Many materials containing Eu^{3+} have been selected as promising candidates for red phosphors, because their $^5D_0$-$^7F_2$ transitions located in a noncentro-symmetric site contribute to better color purity than other phosphors with broad emission bands. More and more attentions have been paid to Eu^{3+} doped vanadates ($Ca_9La(VO_4)_7:Eu^{3+}$),[9] tungstates ($SrWO_4:Eu^{3+}$),[10] titanates ($Na(Gd,Y)TiO_4:Eu^{3+}$),[11] Molybdates ($Bi_2MoO_6:Eu^{3+}$),[12] which shows an effective f-f transition of Eu^{3+} under excitation in the UV spectral region. Due to the outstanding thermal stability, stabilization of ionic charge in the lattice and strong absorption band in the (near) ultraviolet region, rare earth-doped phosphate optical materials have been paid much attention in recent years.[13,14] It is well known that β-$Ca_3(PO_4)_2$ is a typical member of phosphate family which is iso-structural to the nature mineral whitlockite $Ca_{18.19}Mg_{1.17}H_{1.62}(PO_4)_{14}$ and crystallized in the space group R3c.[15] The whitlockite β-$Ca_3(PO_4)_2$ compound has six metal sites (M1-6) in the crystal lattice: the M1-M2 sites are coordinated by eight oxygen atoms, the M3 and M5 sites are surrounded by nine and six oxygen atoms, and the M4, M6 sites are vacant.[16,17] Since there is interesting crystal chemistry and adjustable crystal field environment, many studies have focused on the study of the β-$Ca_3(PO_4)_2$ type compound, such as $Ca_9In(PO_4)_7$, $(Ca,Mg,Sr)_9Y(PO_4)_7:Eu^{2+},Mn^{2+}$, $Ca_9(Al,Lu)(PO_4)_7:Eu^{3+}$,[18-20] especially on the different crystallographic occupancies and the corresponding phase formations. The presence of this particular structure suggests a possible method by which the lattice can accommodate other

School of Materials Science and Engineering, Changchun University of Science and Technology, Changchun 130022, China
E-mail: mixiaoyun@126.com; Fax: +86-431-85583015; Tel: +86-431-85583188
See DOI: 10.1039/x0xx00000x

cations with similar radii and charges without significant changes to the structural frame.

Wet chemistry processes, such as hydrothermal synthesis,[21] coprecipitation[22] and colloidal chemistry[23] are extensively used to obtain desired rare earth-doped phosphors, because the starting materials in these methods can be mixed at molecular level and the reaction temperature is low. To the best of our knowledge, few papers has been published on synthesis, morphology and luminescence properties of $Ca_9Eu(PO_4)_7$ and $Ca_9Eu_{1-x}Ln_x(PO_4)_7$(Ln= Gd, La, Y) phosphors prepared by a facile hydrothermal process.

In this work, the red-emitting $Ca_9Eu(PO_4)_7$ phosphor was synthesized by the hydrothermal method, and the novel material was investigated systematically on structure, photoluminescence excitation and emission spectra as well as the influences of introducing Ln^{3+} (Ln= Gd, La, Y) on the luminescence properties of $Ca_9Eu_{1-x}Ln_x(PO_4)_7$. Three kinds of Eu^{3+} sites in the host were observed via the GSAS structural refinement method. The formation process and shape evolution mechanism of as-prepared $Ca_9Eu(PO_4)_7$ phosphors under different pH conditions were also investigated. The results indicated that the as-prepared phosphors could be a promising red phosphor used in white light-emitting diodes under ultraviolet/near-ultraviolet LED excitation.

2. Experimental

2.1 Materials

Eu_2O_3 (99.99%), Y_2O_3 (99.99%), La_2O_3 (99.99%) and Gd_2O_3 (99.99%) were purchased from Shanghai Sinopharm Chemical Reagent Company. $Ca(NO_3)_2{\cdot}4H_2O$ (A,R), H_3PO_4 (A,R), HNO_3(A,R) and ammonia(A,R) were purchased from Beijing Chemical Company. All chemicals were analytical grade reagents and were used directly without further purification.

2.2 Preparation

A series of polycrystalline $Ca_9Eu(PO_4)_7$ and $Ca_9Eu_{1-x}Ln_x(PO_4)_7$ (Ln= Gd, La, Y) samples were prepared by the hydrothermal process. $Ca_9Eu_{1-x}Ln_x(PO_4)_7$ nanophosphors were synthesized as the following steps: stoichiometric Eu_2O_3 and Ln_2O_3 were dissolved in HNO_3 solution at 80°C with continuous magnetic stirring. After the Eu_2O_3 and Ln_2O_3 were completely dissolved, the extra HNO_3 solution was removed by evaporation. Then deionized water were added to obtain $Eu(NO_3)_3$ and $Ln(NO_3)_3$ solution, respectively. Meanwhile, appropriate amounts of $Ca(NO_3)_2{\cdot}4H_2O$ were dissolved in deionized water. The $Eu(NO_3)_3$, $Ln(NO_3)_3$ and $Ca(NO_3)_2$ solutions were mixed homogeneously under magnetic stirring while stoichiometric H_3PO_4 solution was being added. The pH values were adjusted to about 3,5,7,9 with ammonia solution. Then the precipitates were transferred into four Teflon-lined stainless-steel autoclaves with a filling capacity of 80%, and heated to a given temperature and held for 24h. The autoclaves were cooled down to the room temperature. The precipitates were collected by centrifugation, and washed three times with distilled water. After drying in air at 80°C for 24h, the white powder were transferred to muffle furnace annealing for 2h, the final products were obtained. The $Ca_9Eu(PO_4)_7$ powder was synthesized by the same procedure with the corresponding starting materials.

2.3 Characterization

Powder X-ray diffraction (XRD) patterns were collected by using Cu Kα radiation (λ= 1.54056 Å) on a RigakuD/max-II B diffractometer, operating at 40 kV and 40 mA. The structure refinement was done using the General Structure Analysis System (GSAS) program.[24] The surface morphology of the powder was analyzed by a Hitachi S4200 Scanning Electron Microscopy (SEM). Transmission electron microscopy (TEM) images were obtained using a TECNAI G2 transmission electron microscope operating at 200 kV. The photoluminescence (PL) measurements were performed on a Hitachi F-7000 spectrophotometer equipped with a 150W xenon lamp as the excitation source. The photoluminescence quantum yields (QYs) were measured by absolute PL quantum yield measurement system C9920-02. The luminescence decay curves were obtained from a LeCroy Wave Runner 6100 digital oscilloscope (1 GHz) using a tunable laser (pulse width= 4 ns, gate= 50 ns) as the excitation (Continuum Sunlite OPO) source.

3. Results and discussion

3.1 Phase Identification and Structural Characteristics

$Ca_9Eu(PO_4)_7$ has the similar whitlockite-type structure to β-$Ca_3(PO_4)_2$ with no inversion symmetry.[16] Figure 1 shows the representative XRD patterns of $Ca_9Eu_{1-x}Ln_x(PO_4)_7$ (Ln= Gd, La, Y) samples synthesized by the hydrothermal method at 150℃ for 24h. It is obvious that all the diffraction peaks of these samples can be assigned to the pure whitlockite-type structure with JCPDS card no.46-0402, which indicates that the obtained samples are single phase and the introduced Gd^{3+}, La^{3+}, Y^{3+} don't cause any significant changes of host structure. However, there is a small shift to high diffraction degrees, which is due to the differences of ionic radius between Eu^{3+} and other rare earth ions ($r_{La^{3+}}$>$r_{Eu^{3+}}$>$r_{Gd^{3+}}$> $r_{Y^{3+}}$).[25,26] The ionic radii of Gd^{3+} (1.053 Å, CN= 8), Y^{3+} (1.019 Å, CN= 8), and La^{3+} (1.300 Å, CN= 8) are similar to Eu^{3+} (1.07 Å, CN= 8; 0.947 Å, CN= 6), respectively.[27] Therefore, on the basis of charge and effective ionic radii of cations with different coordination

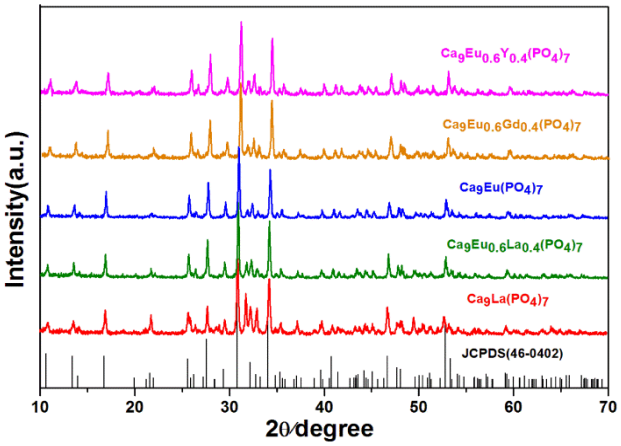

Figure. 1 Representative XRD patterns of the samples.

numbers, it can be expected that the doped Ln^{3+} would occupy similar lattice sites to Eu^{3+} distributing in the host structure. These results indicate that Ln^{3+} are undoubtedly doped into the $Ca_9Eu(PO_4)_7$ crystal lattice.

To determine the structure of the as-prepared phosphor, Rietveld structural refinement was performed for the $Ca_9Eu(PO_4)_7$ with the powder diffraction data. The experimental and calculated diffraction XRD profiles for the $Ca_9Eu(PO_4)_7$ are illustrated in Figure 2. We choose the starting model in this work to be built with crystallographic data taken from the structure of $Ca_9La(PO_4)_7$ (ICSD-83401) belonging to R3c symmetry whose crystal structure is identical with that of $Ca_9Eu(PO_4)_7$.[17,28,29] This calculation refinement using the Rietveld method evidences an excess of electron density due to the presence of heavier europium on sites Ca1, Ca2 and Ca3. However, Ca5 seems to be all-calcium as shown in table 1. From Figure 2 and Table 1, it is observed that experimental data is consistent with calculating data. The synthesized phosphor crystallized in trigonal system. Space group is R3c (No. 161) with Z= 6. As expected, the refined unit cell parameters are a= 10.45140 Å, c= 37.44119 Å, and V= 3541.84 $Å^3$ (Table 1), which matches well with those reported in the literature.[30] Therefore, structure parameters for $Ca_9Eu(PO_4)_7$ as determined by Rietveld refinement of powder XRD data are identical with its real situation.

Figure 3 shows the crystal structure of sample and the local coordination of Ca/Eu with the O atoms of $Ca_9Eu(PO_4)_7$, respectively. The structure of $Ca_9Eu(PO_4)_7$ is consisted of $[PO_4]$ tetrahedrons and Ca/Eu atoms filled in the space between the tetrahedral groups. The coordination numbers of three Ca/Eu atoms are 8, 8, 9 for Ca1(Eu1), Ca2(Eu2) and Ca3(Eu3), respectively. As shown in Table1, the Eu^{3+} are randomly distributed on three individual Ca crystallographic sites.

3.2 Morphology of $Ca_9Eu(PO_4)_7$ in the conditions of different pH values

SEM and TEM images can provide direct information on the shapes and sizes of crystals grown under different experimental conditions. Figure 4 shows SEM and TEM images of $Ca_9Eu(PO_4)_7$ products prepared at different pH values. As shown in figure, there were significant differences in the morphology and crystallite sizes of these $Ca_9Eu(PO_4)_7$ powders by adjusting the pH value from 3 to 9. With the pH value increasing from 3 to 7, the morphologies of samples are mainly composed of a great deal of uniform nano-rods whose average length becomes smaller and smaller. The average length decreases from ~200nm (pH=3) to ~150nm (pH=5), eventually to ~100 (pH=7). Meanwhile, the aspect ratio (ratio of long-axis length to width) also decreases from 5.3 (pH=3) to 4.7 (pH=5), finally to 2.5 (pH=7). In addition, we observe that the number of nano-spherical grains increases slightly along with the increase of pH values. When the pH value reaches to 9, the morphology of samples mainly exists in the form of nano-spherical grains, while seldom exists in the form of nano-rods whose average length and width are ~60nm and ~40nm, respectively. All the experimental parameters were invariable in the experimental process except for the pH value; in other words, the pH value plays a key role in the formation of various morphologies of $Ca_9Eu(PO_4)_7$ phosphors.

The results could be caused by Ostwald ripening process during the hydrothermal synthesis.[31] The synthesis mainly contains two steps; On the first step of the synthesis, small spherical nanocrystallites are formed. In acid media, it is easier for initial ions to transfer from smaller particles to bigger ones. Thus it can lead to growth of the crystals in a certain direction on the second step (in the autoclave). As shown in SEM and TEM images, with the pH value increasing, both anisotropic grain growth tendency and aspect ratio decrease obviously. That indicates the pH value plays a key role in the formation of $Ca_9Eu(PO_4)_7$ morphologies. It may be because the formation process of $Ca_9Eu(PO_4)_7$ is controlled by three reactions as follows:

$$H_nPO_4^{(3-n)-} \leftrightarrow PO_4^{3-} + nH^+ \quad (1)$$

$$M^{n+} + nPO_4^{3-} \leftrightarrow M_3(PO_4)_n \ (M= \text{metal cation}) \quad (2)$$

$$Ca_3(PO_4)_2 + EuPO_4 \leftrightarrow Ca_9Eu(PO_4)_7 \quad (3)$$

When pH is 3, the higher H^+ concentrations restrain the formation of $(PO_4)^{3-}$, which leads to the relatively lower growth rate of $M_3(PO_4)_n$ and $Ca_9Eu(PO_4)_7$. In the high H^+ concentration condition, higher metal cation concentrations and faster ion motions are favorable for anisotropic growth and the product of 1D nano-rods.[32,33] With increasing the pH value, the

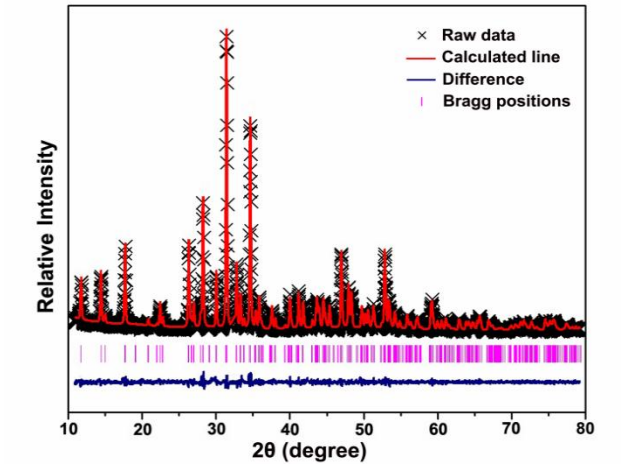

Figure. 2 Rietveld refinement X-ray diffraction patterns of $Ca_9Eu(PO_4)_7$ preparing at pH 7.

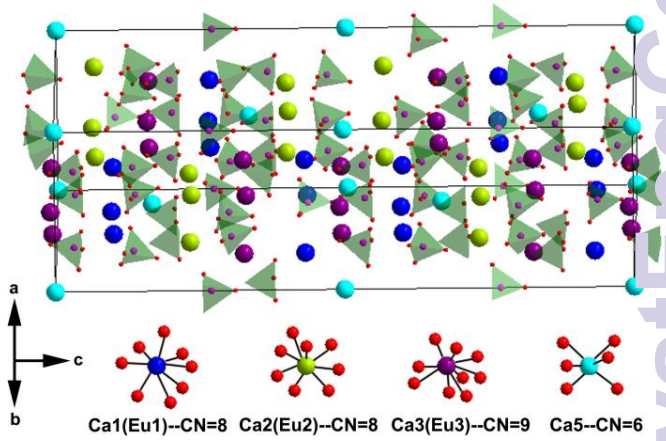

Figure. 3 The crystal structure of $Ca_9Eu(PO_4)_7$ sample and coordination conditions of Ca^{2+} and Eu^{3+}.

Table 1 Refinement results and crystal structure data for $Ca_9Eu(PO_4)_7$

Sample	$Ca_9Eu(PO_4)_7$				
Crystal system	Trigonal				
Space group	*R3c*				
Z	6				
a(Å)	10.45140				
c(Å)	37.44119				
V(Å^3)	3541.84				
Rwp	12.08%				
Rp	8.23%				
χ^2	1.62				
Atom	Wyck	*x/a*	*y/b*	*z/c*	Occupancy
Ca1/Eu1	18b	0.7172540	0.8524360	0.4272390	0.986/0.014
Ca2/Eu2	18b	0.6179690	0.8150200	0.2304400	0.958/0.042
Ca3/Eu3	18b	0.1263440	0.2661140	0.3214350	0.889/0.111
Ca5	6a	0.0000000	0.0000000	-0.0077040	1.0
P1	6a	0.0000000	0.0000000	0.2667840	1.0
P2	18b	0.6803160	0.8398290	0.1267580	1.0
P3	18b	0.6584120	0.8331250	0.0255460	1.0
O1	6a	0.0000000	0.0000000	0.3031630	1.0
O2	18b	0.0100950	0.8772410	0.2477150	1.0
O3	18b	0.7383400	0.8955350	0.1675670	1.0
O4	18b	0.7727570	0.7606730	0.1131180	1.0
O5	18b	0.7450090	0.9828010	0.1058010	1.0
O6	18b	0.5179230	0.7702850	0.1180660	1.0
O7	18b	0.6015310	0.9449090	0.0379410	1.0
O8	18b	0.5626580	0.6871570	0.0426900	1.0
O9	18b	0.8158220	0.9196250	0.0352600	1.0
O10	18b	0.6460740	0.8530020	0.9848450	1.0

decreasing metal cation concentrations and slower ion motions are not conducive to growth of the crystals in a certain direction. Consequently nano-rods having lower aspect ratio and small spherical nanocrystallites are obtained. In alkaline media, the solution has a high $(PO_4)^{3-}$ concentration, but transfer of the ions can't take place easily due to metal ions forming insoluble hydroxides.[34] Therefore, there are a small number of nano-rods and a large number of small spherical nanocrystallites appearing at pH 9. In a word, the pH value plays a crucial role in the formation of crystal morphologies. Based on above analysis, the formation process and shape evolution mechanism of $Ca_9Eu(PO_4)_7$ samples can be depicted graphically in Figure 5.

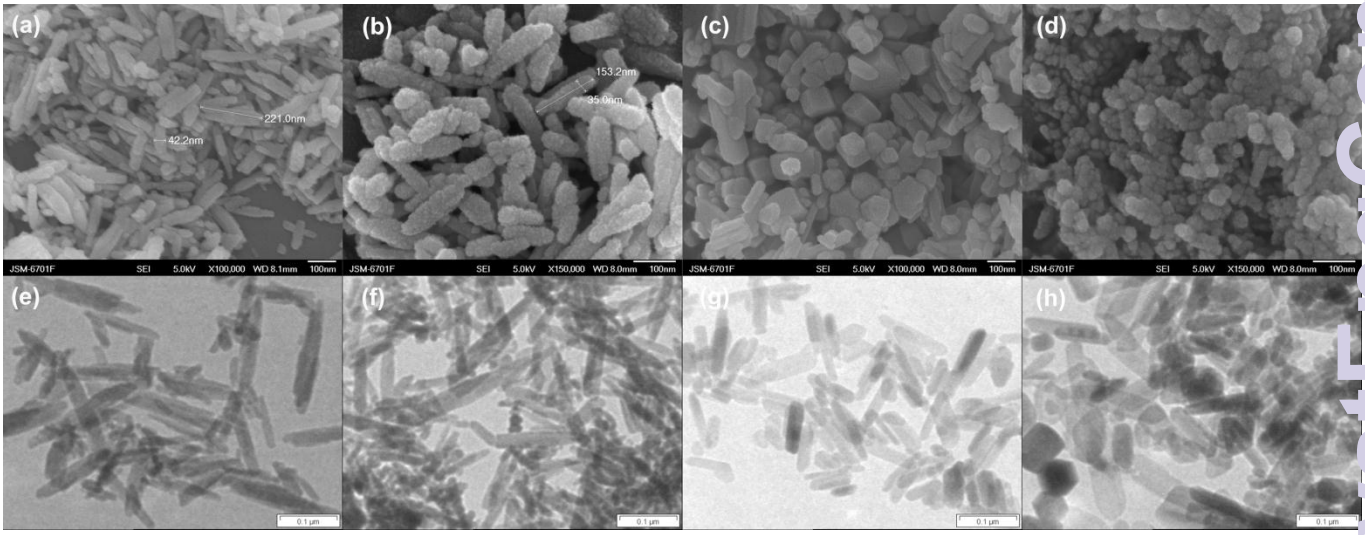

Figure. 4 (a-d) Typical SEM images of $Ca_9Eu(PO_4)_7$ phosphor prepared at different pH values: (a) pH=3, (b) pH=5, (c) pH=7, (d) pH=9. (e-h) Typical TEM images of $Ca_9Eu(PO_4)_7$ phosphor prepared at different pH values: (e) pH=3, (f) pH=5, (g) pH=7, (h) pH=9.

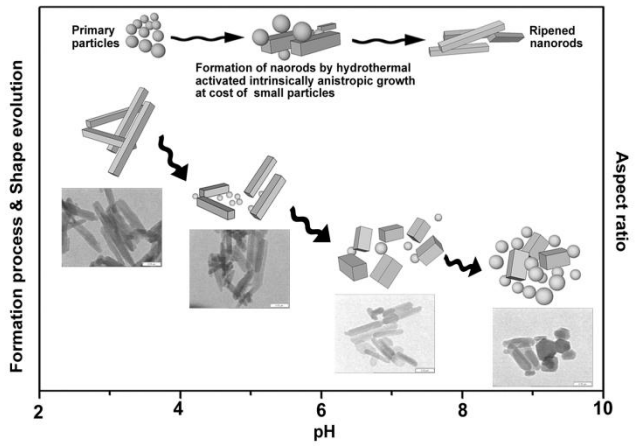

Figure. 5 The Schematic illustration of $Ca_9Eu(PO_4)_7$ formation process and shape evolution mechanism produced by hydrothermal crystallization in the conditions of different pH values.

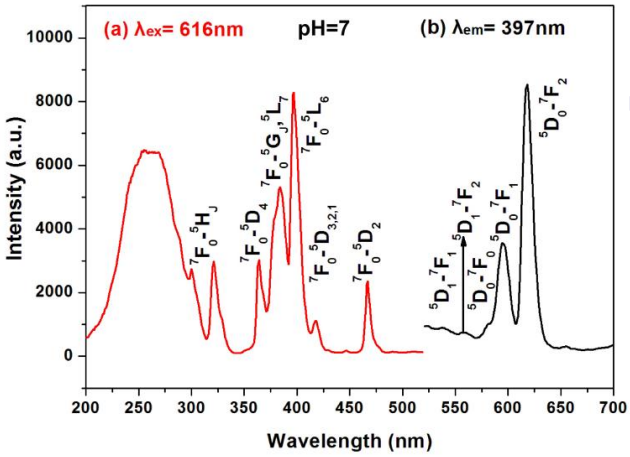

Figure. 6 (a) The excitation spectrum of the red-emitting phosphors $Ca_9Eu(PO_4)_7$ prepared at pH 7 (λ_{em}=616nm) (b) the emission spectrum of $Ca_9Eu(PO_4)_7$ prepared at pH 7 (λ_{ex}=397nm).

3.3Luminescence properties

Photoluminescence spectrums of the red-emitting $Ca_9Eu(PO_4)_7$ phosphor are shown in Figure 6. Figure 6(a) shows excitation spectrum by monitoring $^5D_0 \rightarrow {}^7F_2$ transition of Eu^{3+} at 616nm. A broad band and some sharp lines from the characteristic intra-configurational 4f-4f transitions: $^7F_0 \rightarrow {}^5L_6$ (397nm) and $^7F_0 \rightarrow {}^5D_2$ (467nm) transitions. The broad absorption band from 200nm to 280nm can be attributed to the charge-transfer from the negative ion O^{2-} ($2p^6$) to the empty state of $4f^7$ of Eu^{3+} [ligand-to-metal charge-transfer (CT)]. A suitable red-emitting UV-LED phosphor should exhibit absorption around 400nm (LED excitation wavelength). It is clear that the excitation has a strong absorption band locating near 400nm, which can be excited by the radiation of near UV-emitting InGaN based LED chips. As shown in Figure 6(b), emission spectrum under 397nm excitation consists of five sharp lines ranging from 530 to 650nm with peaks at 535nm ($^5D_1 \rightarrow {}^7F_1$), 556nm ($^5D_1 \rightarrow {}^7F_2$), 581nm ($^5D_0 \rightarrow {}^7F_0$), 596nm ($^5D_0 \rightarrow {}^7F_1$), and 616nm ($^5D_0 \rightarrow {}^7F_2$). The emission spectrum of $Ca_9Eu(PO_4)_7$ is composed of several sharp emissions from both the lowest excited $^5D_0$ and the higher energy levels $^5D_1$ of Eu^{3+}. The presence of emission lines from higher excited states $^5D_1$ is attributed to the low vibration energy of $(PO_4)^{3-}$ groups. The multiphonon relaxation by $(PO_4)^{3-}$ is not enough to bridge the gaps between the higher energy levels $^5D_1$ and the $^5D_0$ level of Eu^{3+} completely, leading to weak emissions from these levels.[20] The emission from the upper levels ($^5D_1$, $^5D_2$, and $^5D_3$) can hardly be observed in other Eu^{3+} doped oxides, silicates and borates whose maximum vibration energies are higher than $(PO_4)^{3-}$ groups.[35] The major red emission peak located at 616nm is attributed to the electric dipole transition $^5D_0 \rightarrow {}^7F_2$. This electric-dipole transition is parity forbidden f-f configuration transition, which would only occur when Eu^{3+} occupy lattice sites without inversion symmetry. The electric dipole transition ($^5D_0 \rightarrow {}^7F_2$) is more sensitive to the environment than magnetic dipole transition ($^5D_0 \rightarrow {}^7F_1$) which is not much affected by ligand field around Eu^{3+}.[36] Thus, the $^5D_0 \rightarrow {}^7F_2$ transition is dominated if Eu^{3+} ions occupy a non-centrosymmetric position, while the $^5D_0 \rightarrow {}^7F_1$ transition is dominated when Eu^{3+} occupy a centrosymmetric position. The value of $R=I(^5D_0 \rightarrow {}^7F_2)/I(^5D_0 \rightarrow {}^7F_1)$ can demonstrate the site symmetry substituted by Eu^{3+}. Meanwhile, the value of R is a key index reflecting the chromaticity and saturation of red color. Generally, the larger the ratio of $I(^5D_0 \rightarrow {}^7F_2)/I(^5D_0 \rightarrow {}^7F_1)$ is, the closer to the optimal value of the color chromaticity.[20,37] In our work, R belonging to $Ca_9Eu(PO_4)_7$ sample is calculated to 2.4, which indicates a low symmetry of Eu^{3+} site. The value of R is quite large in comparison with those of the other Eu^{3+}-doped phosphates ($GdPO_4$, $LaPO_4$, YPO_4)[38,39], which demonstrates that the ratio is favorable to improve the color purity of the red phosphor.

The 4f orbits of Gd^{3+}, La^{3+}, Y^{3+}, are half-filled, full-filled, or empty. Due to these ions having no fluorescence properties, they can be used as matrix material. Moreover, Emission intensity of phosphor is significantly affected by the concentration of doping rare earth ions; thus, the emission intensities for the $Ca_9Eu_{1-x}Ln_x(PO_4)_7$(Ln= Gd, La, Y) as a function of Ln^{3+} concentrations have been investigated. The emission (λ_{ex}=397nm) spectrums of $Ca_9Eu_{1-x}Ln_x(PO_4)_7$ (Ln= Gd, La, Y) phosphors doped with various Ln^{3+} concentrations are shown in Figure 7(a)-(c); Figure 7(d)-(f) show dependence curves with error bars of emission intensities on the concentration of Ln^{3+}, respectively. As shown in the figure, with concentrations of Ln^{3+} increasing, the emission intensity of Eu^{3+} decreases, but the profiles of the emission spectrum have no obvious changes. When Ln^{3+} replaces Eu^{3+} completely, emission intensities reach the minimum. In other words, with the increases of Eu^{3+} concentrations, luminescence intensities increase nearly linearly and the concentration quenching of Eu^{3+} is not observed in $Ca_9Eu_{1-x}Ln_x(PO_4)_7$ (Ln= Gd, La, Y) samples.

There are two main reasons of no concentration quenching effect of Eu^{3+}. In the Van Uiter-Johnson model,[40] the concentration quenching of Eu^{3+} is not possible by a simple multipolar transfer process since energy difference between

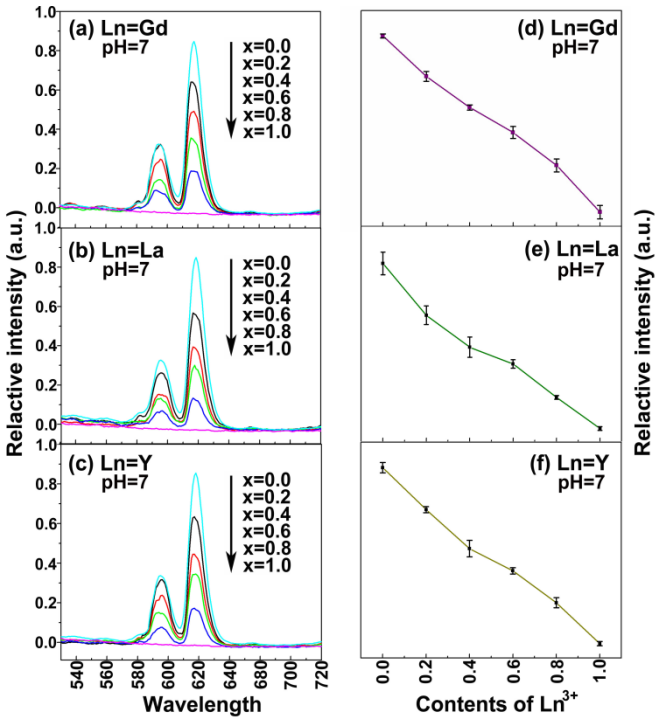

Figure. 7 (a-c) Emission (λ_{ex}=397nm) spectra of $Ca_9Eu_{1-x}Ln_x(PO_4)_7$(Ln= Gd, La, Y) phosphors doped with various Ln^{3+} concentrations in the condition of pH 7; and (d-f) the dependence curves with error bars of emission intensity on the concentration of Ln^{3+} in the condition of pH 7.

the $^5D_0$ and $^7F_6$ levels far exceeds that between $^7F_6$ and $^7F_0$ levels. Therefore, the concentration quenching is due to the exchange interaction between Eu^{3+}. Under this circumstance, crystal structure plays a key role in the energy transfer depending on non-resonant mechanism. This means if Eu^{3+} is separated by more than one ion, relative weak effect impacting on each other will lead to the phenomenon of no concentration quenching. On the other side, in the Blasse model,[41] if the Eu^{3+} sites are separated by more than one intermediary separating Eu^{3+} at 90° and 180°, the overlap between Eu^{3+} will occur and concentration quenching will have possibilities to take place. In our research, the as-prepared $Ca_9Eu_{1-x}Ln_x(PO_4)_7$(Ln= Gd, La, Y) phosphors had whitelockite-type crystal structure and Eu^{3+} together with Ca^{2+} located at Ca1, Ca2, and Ca3 sites. As shown in Figure 3, Eu^{3+} of the samples are separated well by the intermediary (PO_4 tetrahedra), whose Eu-O-P and P-O-P angles are far from 90° and 180°. The fact means that there is no overlap of the wave function between Eu^{3+}. Therefore, no concentration quenching is observed in this phosphor.

As shown in figure 8, photoluminescence decay curves of the Eu^{3+} in $Ca_9Eu_{0.6}Ln_{0.4}(PO_4)_7$(Ln= Gd, La, Y) were measured with an excitation at 397nm and monitored at 616nm. The decay curves for $Ca_9Eu_{1-x}Ln_x(PO_4)_7$(Ln= Gd, La, Y) samples can be well fitted into single-exponential function as:[34]

$$I=I_0 \exp(-t/\tau) \quad (4)$$

where I_0 and I are the luminescence intensities at time 0 (initial intensities) and t, respectively, and τ is the decay lifetime. On

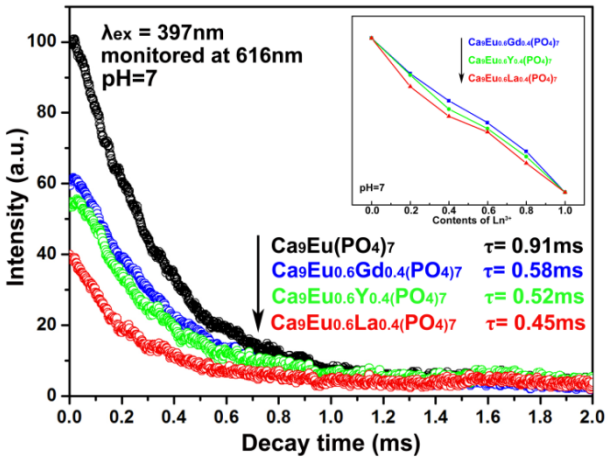

Figure. 8 The decay curves of $Ca_9Eu(PO_4)_7$ and $Ca_9Eu_{0.6}Ln_{0.4}(PO_4)_7$ (Ln= Gd, La, Y) prepared at pH 7 under excitation of 397nm.

the basis of eqn (4), the lifetime values of $Ca_9Eu(PO_4)_7$, $Ca_9Eu_{0.6}Gd_{0.4}(PO_4)_7$, $Ca_9Eu_{0.6}La_{0.4}(PO_4)_7$ and $Ca_9Eu_{0.6}Y_{0.4}(PO_4)_7$, were determined to be 0.91, 0.58, 0.45 and 0.52ms, respectively. The value of τ is directly reflected by photo-luminescence intensity. Generally, the longer lifetime of samples own, the higher luminescence intensities have. As shown in the inset of figure 8, the variation tendency of luminescence intensity is consistent with the variation of lifetime. The luminescence intensity of $Ca_9Eu_{0.6}Gd_{0.4}(PO_4)_7$ sample owns the longest lifetime than others. The decrease of emission intensity should be caused by the decrease of Eu^{3+} concentration in $Ca_9Eu_{1-x}Ln_x(PO_4)_7$. There exists such an order of the ability to decrease the emission intensity: $Gd^{3+}<Y^{3+}<La^{3+}$ ($R_{La}>R_{Gd}>R_Y$).[25,42] This can be attributed to the larger Ln^{3+} can dilute the concentration of Eu^{3+} more efficiently than the smaller ones. However, Gd^{3+} doesn't follow the same law as Y^{3+}, and La^{3+} in $Ca_9Eu_{1-x}Ln_x(PO_4)_7$. This can be attributed to the energy transfer progress between Gd^{3+} and Eu^{3+}.[43,44] Therefore, the intensity of $Ca_9Eu_{1-x}Gd_x(PO_4)_7$ phosphor is higher than that of $Ca_9Eu_{1-x}Ln_x(PO_4)_7$ (Ln= Y^{3+}, La^{3+}). Upon excitation at a wavelength of 397nm, the PL quantum yields of $Ca_9Eu(PO_4)_7$, $Ca_9Eu_{0.6}Gd_{0.4}(PO_4)_7$, $Ca_9Eu_{0.6}La_{0.4}(PO_4)_7$ and $Ca_9Eu_{0.6}Y_{0.4}(PO_4)_7$ samples were determined to be 40.8%, 24.3%, 19.7% and 21.9%, respectively.

Figure 9 shows photoluminescence excitation and emission spectrums of $Ca_9Eu(PO_4)_7$ as a function of different pH values. The spectral profiles of samples with different morphologies are basically similar. This is because the excitation and emission from the f-f transitions within $4f^6$ configuration are shielded very well by $5s^2$ and $5p^6$ orbits. Therefore, peak positions of excitation and emission are hardly affected by the changing morphologies of host lattices. However, there are dramatically different in the PL intensities of $Ca_9Eu(PO_4)_7$ with the four different pH values. In brief, the highest relative luminescence intensity appears in the sample prepared at pH 7 (blue line), while the lowest relative luminescence intensity emerges in the condition of pH 9 (black line), and the relative intensity of the former is much higher than that of the latter.

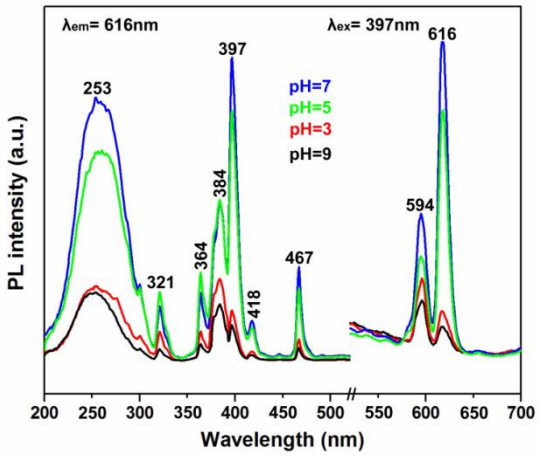

Figure. 9 Excitation and emission spectra of $Ca_9Eu(PO_4)_7$ samples with different pH values (pH=3, 5, 7, 9).

As is well-known, there are many factors affecting photoluminescence properties of nano-particles, such as surface defects, surface states, specific surface area and crystalline states.[45] These factors may provide non-radiative recombination routes for electrons and holes, which can decrease luminescence intensity drastically. In order to obtain the phosphors as efficient as possible, the number of electron/hole recombinations going by optically active centers must be maximized.[46] As shown in figure 4, the sample preparing at pH 7 has smooth surfaces, fewer defects and better crystalline state. Therefore, it could be the reason that the luminescence intensity of $Ca_9Eu(PO_4)_7$ sample preparing at pH 7 is higher than other samples.

Conclusions

In summary, we have synthesized the novel red-emitting $Ca_9Eu(PO_4)_7$ phosphate phosphor by the hydrothermal method. Rietveld refinement of powder X-ray diffraction patterns of $Ca_9Eu(PO_4)_7$ demonstrated that the structure of $Ca_9Eu(PO_4)_7$ consisted of $(PO_4)^{3-}$ tetrahedra, and Ca/Eu atoms filled in the space between the tetrahedral groups, with Eu^{3+} distributing randomly on three individual Ca crystallographic sites. The major red emission peak located at 616nm under 397nm excitation attributed to the electric dipole transition $^5D_0 \rightarrow {}^7F_2$ of Eu^{3+} was a parity forbidden f-f configuration transition, which would only occur when Eu^{3+} occupied lattice sites without inversion symmetry. The introduction of Gd, La, Y ions into sample made luminescence properties of $Ca_9Eu_{1-x}Ln_x(PO_4)_7$ (Ln= Gd, La, Y) phosphors decrease. Moreover, no concentration quenching effects were observed in $Ca_9Eu_{1-x}Ln_x(PO_4)_7$ (Ln= Gd, La, Y) samples. By means of SEM and TEM analysis, we discovered that the pH value in the initial reaction solution played a key role in the formation of $Ca_9Eu(PO_4)_7$ nanophosphor morphologies. With pH values increasing in the initial reaction solution, the morphologies of samples changed from rods to spheres and their aspect ratios decreased at the same time. Different morphologies determined different photo-luminescence properties, and samples prepared at pH 7 manifested better photoluminescence properties relative to other samples. Therefore, a potential red-emitting phosphor might be promising to be applied in white light-emitting diodes.

Acknowledgements

This research was financially supported by the Scientific and Technological Department of Jilin Province (Grant Nos. 20130522176JH and 20130102016JC), and the National Natural Science Foundation of China (Grant No. 61307118).

Notes and references

1 Y. S. Tang and S. F. Hu, *Appl. Phys. Lett.*, 2007, **90**(15), 151-108.
2 F. H. Wang, D. Z. Zhou, S. Y. Ma, H. W. Yu, P. L. Li and P. Yang, *J. Alloy. Compd.*, 2011, **509**(14), 4824-4826.
3 Y. Liu, X. Zhang, Z. Hao, X. Wang and J. Zhang, *Chem. Commun.*, 2011, **47**, 10677-10679.
4 J. S. Kim, P. E. Jeon, Y. H. Park, J. C. Chol, H. L. Park, G. C. Kim and T. W . Kim, *Appl. Phys. Lett.*, 2004, **85**(17), 3696.
5 A. A. Setlur, W. J. Heward, Y. Gao, A. M. Srivastava, R. G Chandran, and M. V. Shankar, *Chem. Mater.*, **18**(2006), 3314.
6 Y. Tian, R. N. Hua, B. J. Chen, N. S. Yu, W. Zhang and L. N. Na, *CrystEngComm*, 2012,**14**, 8110-8116.
7 Neeraj, N. Kijima, and A. K. Cheetham, *Chem. Phys. Lett.*, 2004, **387**, 2-6.
8 Y. Q. Li, A. C. A. Delsing, G. de With and H. T. Hintzen, *Chem. Mater.*, 2005, **17** (12), 3242-3248.
9 L. H. Liu, R. J. Xie, N. Hirosaki, Y. Q. Li and T. Takeda, C. N. Zhang, J. G. Li and X. D. Sun, *J. Am. Ceram. Soc.*, 2010 **93,** 4081-4086.
10 Maheshwary, B. P. Singh, J. Singh and R. A. Singh. *RSC Adv.*, 2014, **4**, 32605-32621.
11 L. K. Bharat and J. S. Yu, *CrystEngComm*, 2015,**17**, 4647-4653
12 J. J. Zhang, Y. L. Liu, L. L. Li, N. N. Zhang, L. C. Zou and S. C. Gan. *RSC Adv.*, 2015, **5**, 29346-29352.
13 J. C. Zhang, Y. Z. Long, H. D. Zhang, B. Sun, W. P. Han and X. Y. Sun, *J. Mater. Chem. C.*, 2014, **2**, 312-318.
14 V. Bedekar, D. P. Duttal, M. Mohapatra, S. V. Godbole, R. Ghildiyal and A. K. Tyagi, *Nanotechnology*, 2009, **20**, 125707.
15 B. I. Lazoryak, T. V. Strunenkova, V. N. Golubev, E. A. Vovk and L. N. Ivanov, *Mater. Res. Bull.*, 1996, **31**, 207.
16 Y. N. Xue, F. Xiao and Q. Y. Zhang, *Spectrochim. Acta Part. A*, 2011, **78**, 1445-1448.
17 A. Bessiere, R. A. Benhamou, G. Wallez, A. Lecointre and B. Viana, *Acta Mater.*, 2012, **60**, 6641-6649.
18 V. A. Morozov, A. A. Belik, S. Y. Stefanovich, V. V. Grebenev, O. I. Lebedev, G. V. Tendeloo, and B. I. Lazoryak, *J. Solid. State. Chem.*, 2002, **165**, 278-288.
19 C. H. Huang, P. J. Wu, J. F. Lee and T. M. Chen, *J. Mater. Chem.*, 2011, **21**, 10489.
20 F. P. Du, Y. Nakai, T. Tsuboi, Y. L. Huang and H. J. Seo, *J. Mater. Chem.*, 2011, **21**, 4669.
21 J. Yang, C. M. Zhang, C. X. Li, Y. N. Yu and J. Lin, *Inorg. Chem.,* 2008, **47**, 7262-7270.
22 C. Lind, A. P. Wilkinson, C. J. Rawn and E. A. Payzant, *J. Mater. Chem.*, 2001, **11**, 3354.
23 A. Huignard, T. Gacoin, J. P. Boilot, *Chem. Mater.*, 2002, **12**, 1090.

24 C. Larson and R. B. Von Dreele, *General Structure Analysis System(GSAS)*, Los Alamos National Laboratory, Los Alamos, NM, 1994, 86-748.
25 P. Boutinaud, L. Sarakha, R. Mahiou, P. Dorenbos, Y. Inaguma, *J. Lumin.*, 2010, **130,** 1725-1729.
26 G. F. Ju, Y. H. Hu, L. Chen, X. J. Wang and Z. F. Mu, *Mater. Res. Bull.*, 2013, **48**, 4743-4748.
27 R. D. Shannon, Acta Crystallogr., Sect. A: Cryst. Phys., Diffr., Theor. Gen. Crystallogr., 1976, **32**, 751.
28 Z. H. Xu, C. X. Li, Z. Y. Hou, C. Peng and J. Lin, *CrystEngComm*, 2011,**13**, 474-482.
29 A. V. Teterskii, S. Yu. Stefanovich, B. I. Lazoryak and D. A. Rusakov, *Russ. J. Inorg. Chem.*, 2007, **52**(3), 308–314.
30 R. A. Benhamou, A. Bessière, G. Wallez, B. Viana, M. Elaatmani, M. Daoud and A. Zegzouti, *J. Solid. State. Chem.*, 2009, **182**, 2319-2325.
31 O. Krichershy and J. Stavan, *Phys. Rev. Lett.,* 1993, **70**, 1473.
32 A. Phuruangrat, N. Ekthammathat, S. Thongtem and T. Thongtem, *Res. Chem. Intermed.*, 2013, **39**, 1363-1371.
33 Y. J. Zhang and H. M. Guan., *J. Cryst. Growth*, 2003, **256**, 156-161.
34 B. Yan and X. Z. Xiao, *J. Nanopart. Res.*, 2009, **11**, 2125-2135.
35 G. Blasse and B. C. Grabmaier, *Lumin. Mater.*, Springer-Verlag, Berlin Heidelberg, 1994, ch. **4** p. 100.
36 C. Gorller-Walrand, K. Binnemans, Rationalization of Crystal-Field Parametrization, Handbook on the Physics and Chemistry of Rare Earths, ed K. A. Gschneidner and L. Eyring, North-Holland, Amsterdam, 1996.
37 Z. W. Zhang, L. Liu, S. T. Song, J. P. Zhang and D. J. Wang, *Curr. Appl. Phys.*, 2015, **15**, 248-252
38 Y. L. Huang and H. J. Seo, *J. Phys. Chem. A*, 2009, **113**, 5317-5323
39 L. X. Yu, D. C. Li, M. X. Yue, J. Yao and S. Z. Lu, *Chem. Phys.*, 2006, **326**, 478-482
40 L. G. Van Uitert and L. F. Johnson, *J. Chem. Phys.*, 1966, **44**, 3514.
41 G. Blasse, *J. Chem. Phys.*, 1967, **46**, 2583.
42 R. Norrestam and M. Nygren. *J. Chem. Mater.*, 1992, **4**(3), 734-743.
43 J. Gopaiakrishnan and A. Manthiram, *J. Chem. Soc., Dalton Trans.*, 1981, **3**, 668-672.
44 X. M. He, L. H. Zhang and G, Chen, *J. Alloy. Compd.*, 2009, **467**(1-2), 366-369.
45 L. Q. Jing, Y. C. Qu, B. Q. Wang , B. J. Jiang and H. G. Fu, *Sol. Energ. Mat. Sol. C.*, 2006, **90**, 1773-1787
46 J. Yang, X. M. Liu, C. X. Li, Z. W. Quan, D. Y. Kong and J. Lin, *J. Cryst. Growth*, 2007, **303**, 480.

Table of Contents

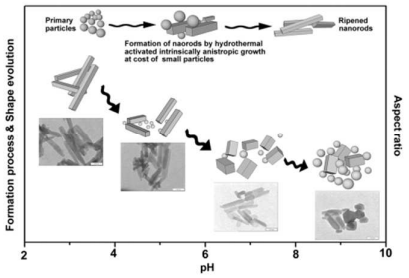

During the hydrothermal synthesis, pH values play a crucial role in the formation of crystal morphologies